ACS NANOSCIENCE Au
AN OPEN ACCESS JOURNAL OF THE AMERICAN CHEMICAL SOCIETY

pubs.acs.org/nanoau
Article

Semiconducting Nanotubes Derived from a Rectangular Graphyne: A DFT Study

Wjefferson Henrique da Silva Brandão, Anderson Gomes Vieira, Jonathan da Rocha Martins, Andrea Latgé, Marcelo Lopes Pereira, Junior, and Eduardo Costa Girão*

Cite This: https://doi.org/10.1021/acsnanoscienceau.5c00157
Read Online
ACCESS | Metrics & More | Article Recommendations

ABSTRACT: Proposing new ways to organize carbon in 2D nanomaterials has been a relevant strategy in the search for systems with targeted properties for different applications. One focus is the study of fully sp^2 nongraphitic networks, with successfully synthesized examples. Hybrid $sp-sp^2$ systems of the graphyne family are a related approach, and many systems have the honeycomb lattice as a base model. However, other examples have been inspired by other lattices as the recently proposed rγGY sheet, which features a semiconducting behavior with highly localized *quasi*-1D states. Here, we investigate how to tune rγGY properties by folding this sheet into nanotube forms. We elucidate mechanisms that determine their electronic structure by means of density functional theory calculations, as well as we identify the interplay involving chirality, diameter, and the emergence of dispersive/localized frontier states on gap modulation through simple extrapolated methods.

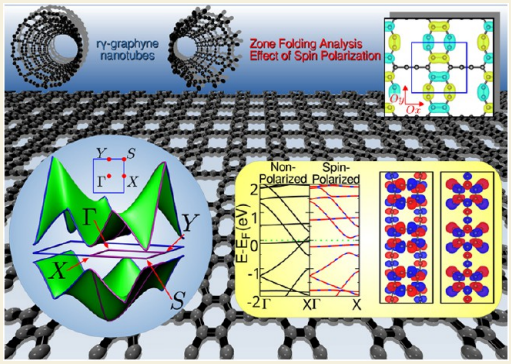

KEYWORDS: *nonconventional graphynes, nanotubes, electronic structure, zone folding, flat states, semiconducting materials*

INTRODUCTION

Fullerenes are usually cast as the starting point of the nanocarbon materials timeline.[1] However, carbon nanotubes were the driving force behind the development of a worldwide scientific community, leading to the broad field of nanocarbons as we know it today.[2−5] While sharing space with graphene[6,7] and other 2D materials[8,9] over the last two decades, nanotubes have remained promising for several applications.[5] They exhibit selectivity to interaction with specific compounds, making them potentially useful for sensors and extraction methods,[10] as well as their electronic properties dependent on curvature and boundary conditions in an intricate way.[11−13] Their geometry is naturally convenient for nanoelectronic applications as both electrodes[14] and active parts of nanodevice setups.[15] Given their relevance, as exemplified by the topic listed above, the relation between the properties of nanotubes and the graphene sheet that makes up the tube walls has emerged as a basic topic in carbon-based textbooks.[16]

Graphene has emerged as one of the most extensively studied nanocarbon materials since the groundbreaking experiments of the early 2000s.[6] Considerable research efforts have focused on tailoring its electronic properties, particularly in strategies aimed at opening a band gap.[17,18] In this context, although carbon nanotubes have been systematically investigated for a longer period, they represent a natural extension of the graphene framework for tuning the physical behavior of the honeycomb lattice. Unlike nanoribbons,[19] whose properties are strongly influenced by edge effects,[20,21] carbon nanotubes preserve the structural integrity of the parent lattice, facilitating direct comparison with the properties of the planar graphene sheet.

Efforts to tailor the electronic properties of nanocarbon materials, especially graphene, date back to the late 1990s, when the idea of engineering new two-dimensional carbon lattices was first proposed.[22] Early ideas on this issue were mainly related to the distribution of extended sets of defects in graphene until a point is reached at which the structure cannot be viewed as defective graphene, but as a new material.[23] These were the Haeckelite structures, which can contain pentagonal and heptagonal rings in addition to the original hexagons of graphene.[24,25] In the following decades, several other proposals for different nanocarbon 2D lattices have been reported, covering a broad range of behaviors.[26] Such studies gained additional motivation, as a nongraphitic lattice was synthesized a few years ago.[27] As the field evolved, such proposals began to involve not only the sp^2 state of carbon, but also atoms with other hybridization states.[28−30] A remarkable

Received: October 21, 2025
Revised: May 28, 2026
Accepted: May 29, 2026

example is the class of graphynes, carbon sheets composed of a combination of sp and sp^2 carbons.[31] They were initially hypothesized from the insertion of acetylenic bridges in substitution of sp^2–sp^2 carbon bonds in graphene, so that different concentrations and different strategies to insert the sp chains result in several distinct graphynes with electronic properties ranging from metallic to Dirac materials and semiconductors.[30,32] In analogy to graphene, the electronic behavior of graphynes can be further tuned by their modification into nanoribbon and nanotube forms.[33−36]

Finally, a more recent trend has been the study of graphyne forms not inspired by graphene, but in other sp^2 2D allotropes of carbon.[37−39] One recent example is a system called rectangular γ-graphyne (rγGY), a graphyne structure that does not have graphene, but 2D biphenylene as its parent sp^2 sheet.[40] The symbol γ in rγGY refers to the fact that it preserves a single hexagonal sp^2 inside its unit cell, with subsequent hexagons connected by acetylenic connections.

The rγGY sheet has been reported as a semiconducting sheet with anisotropic electronic properties, as highly localized states extend along a single crystalline direction of the sheet. In contrast, its frontier states are shown to be adjusted by the size of the acetylenic chains composing the system.[40] Later, rγGY was further studied with a class of other graphyne systems.[41] Here, we follow the analogy with the graphene case and study the electronic properties of rγGY nanotubes (rγGYNTs). We show how the tube properties vary with different chiralities, as well as how they are affected by curvature effects. These tubes are generally semiconductors, but with substantial differences from their 2D counterparts, especially in high-curvature cases. The results are further rationalized by a zone-folding approach that reveals the origins of flat bands present in certain kinds of tubes.

STUDIED SYSTEMS

In Figure 1(a) we illustrate the rγGY sheet, together with its lattice vectors $\mathbf{a}_1 = (a,0)$ and $\mathbf{a}_2 = (0,b)$, where the optimized lattice parameters are a = 6.92 Å and b = 6.28 Å. Considering the original sp^2 2D biphenylene as the starting point, acetylenic bridges are introduced on bonds linking different hexagons

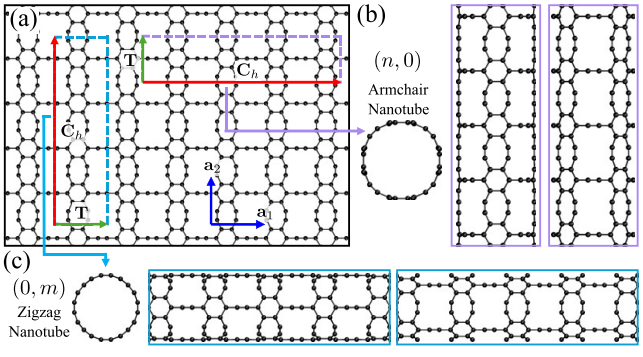

Figure 1. (a) Atomic structure of the rγGY sheet, with its lattice vectors $\mathbf{a}_1$ and $\mathbf{a}_2$ represented by the blue arrows. Here, the projections of the unit cells of the (3,0) and (0,4) tubes over the rγGY sheet are represented by the dashed purple and blue rectangles, while their $\mathbf{C}_h$ ($\mathbf{T}$) vectors are represented by red (green arrows). (b) Example of a (n, 0) nanotube with n = 4 with the cross-section (XY), as well as two side (XZ and YZ) views. (c) Example of a (0, m) nanotube with m = 4 with the cross-section (XY), as well as two side (XZ and YZ) views.

along both the $\mathbf{a}_1$ and $\mathbf{a}_2$ directions. The acetylenic bridges along the $\mathbf{a}_2$ direction are not perfectly linear, and will hereafter be referred to as *curved acetylenic bridges* (or CABs) from rγGY. On the other hand, the chains connecting hexagons along the $\mathbf{a}_1$ direction are perfectly linear and will be referred to as *straight acetylenic bridges* (or simply SABs).

We studied nanotubes based on the rγGY lattice, where the chiral vector defines the folding direction

$$\mathbf{C}_h = n\mathbf{a}_1 + m\mathbf{a}_2 = (n, m) \quad (1)$$

where n and m are integers, in analogy to the well-known case of nanotubes based on graphene. However, due to the rectangular symmetry of rγGY, the range of (n,m) values resulting in distinct nanotube geometries corresponds to n, $m \geq 0$, as far as at least one of the chiral indexes n and m is nonzero. The projection of the nanotube unit-cell over the rγGY sheet is further defined with the aid of a translational vector

$$\mathbf{T} = t_1\mathbf{a}_1 + t_2\mathbf{a}_2 = (t_1, t_2) \quad (2)$$

0 which is also defined in terms of integer t_1 and t_2 coefficients, but in such a way that $\mathbf{C}_h \cdot \mathbf{T} = 0$. It turns out that t_1 and t_2 usually have very high values due to the noninteger ratio between the $\mathbf{a}_1$ and $\mathbf{a}_2$ lattices of rγGY, which makes simulations impractical for arbitrary chiralities. A marked exception corresponds to the high-symmetric (n,0) and (0,m) cases, as their translational vectors are (0,1) and (1,0), respectively. For these reasons, we focus our study on (n,0) and (0,m) nanotubes with n and m ranging from 2 to 12. In Figure 1(b,c), we illustrate examples of a (n,0) and a (0,m) tube, while the projection of their unit cells over the rγGY sheet is represented in Figure 1(a). The (2,0) and (0,2) cases (here considered limiting nanotube structures) feature very small ≈4 Å diameters, the reason for which we exclude hypothetical (1,0) and (0,1), since their diameters would be of the same order as a carbon–carbon bond. In Figure 1(b,c), for examples of the (n,0) and (0,m) nanotubes, we represent the projection of the nanotube's unit cell over 2D rγGY, as well as their cylindrical structures. In analogy to the graphene's case, we call the (n,0) and (0,m) structures as *armchair* and *zigzag* rγGYNTs, a-rγGYNTs and z-rγGYNTs, respectively. These designations follow the alignment of the hexagonal rings of rγGY relative to the nanotube's cross-section.

METHODS

To study the 2D and 1D rγGY systems, we performed simulations based on density functional theory (DFT)[42,43] using the SIESTA code.[44] A double-ζ polarized (DZP) basis set of numerical atomic orbitals[44] was used to expand the wave functions for valence electrons, whereas core electrons were treated through Troullier-Martins pseudopotentials.[45] The reach of the basis set functions was defined in SIESTA by the energy shift parameter, set as 0.05 eV.[46] Exchange-correlation energy has been considered by means of the generalized gradient approximation (GGA) according to the Perdew–Burke–Ernzerhof (PBE) parametrization.[47] The real-space grid used to describe charge density was defined in terms of a 400 Ry mesh cutoff, while reciprocal space integrations were performed with a 40 × 44 × 1 (1 × 1 × 44) [1 × 1 × 40] Monkhorst–Pack sampling for 2D rγGY (armchair rγGYNTs) [zigzag rγGYNTs]. In these periodic-boundary-conditions calculations, vacuum regions of 40 Å were included for all the nonperiodic directions of the 1D and 2D systems to avoid interactions with their periodic images. Structural relaxation was performed for the atomic coordinates by considering a maximum

https://doi.org/10.1021/acsnanoscienceau.5c00157
ACS Nanosci. Au XXXX, XXX, XXX–XXX

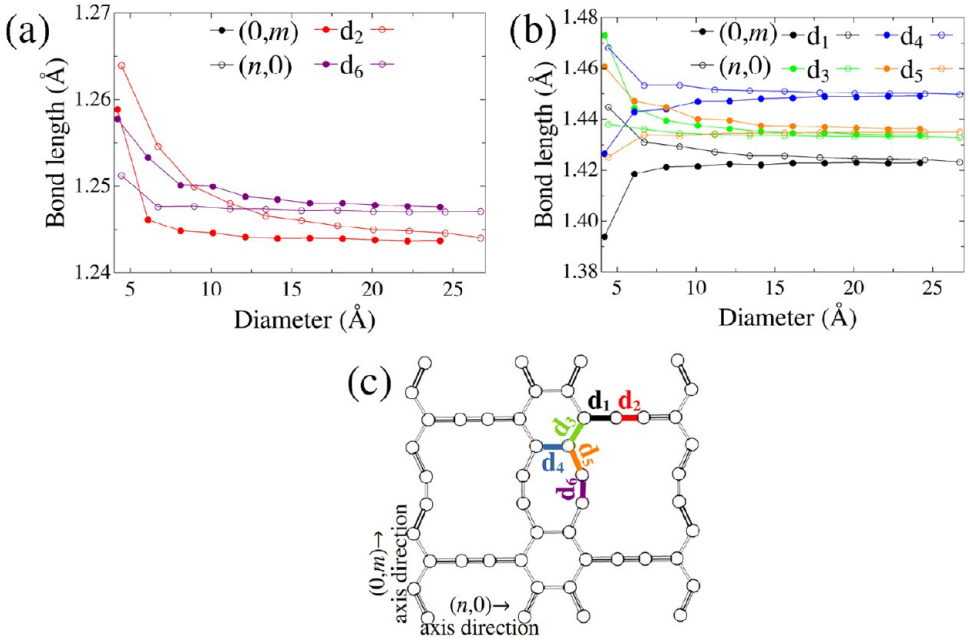

Figure 2. Bond length versus nanotube diameters. (a) sp bonds; (b) sp−sp^2 and sp^2−sp^2. Filled and empty circles denote $(n,0)$ and $(0,m)$ tube families, respectively. (c) Molecular structural network along with the highlighted bonds.

force tolerance of 0.01 eV/Å, and the unit cell vectors were optimized within a maximum tolerance of 0.1 GPa for stress components.

RESULTS

Structural Properties

First, we examined how curvature affects the bond-length profile of the rγGY nanotubes. We computed the bond lengths indicated by d_i, $1 \le i \le 6$ (see Figure 2(c) for their definition), as functions of the tube diameters for both tube chiralities. The results for the two families are shown in Figure 2(a,b). The sp−sp bonds (d_2 and d_6) corresponding to strong triple C≡C bonds, exhibit only minor variations over most diameter ranges (see Figure 2(a)). However, for both $(n,0)$ and $(0,m)$ tubes, a slight elongation is observed at small diameters, as curvature induces deviations from the natural linear geometry of *sp* hybridized carbon, becoming slightly sp^2-like. More pronounced changes are found for the sp−sp^2 (d_1 and d_5) and sp^2−sp^2 (d_3 and d_4) bonds, as shown in Figure 2(b). The rolling direction, either $(n,0)$ or $(0,m)$, directly affects shortening/stretching of specific bond lengths, particularly at small diameters. For example, bonds d_1 and d_4 (black and blue lines) are oriented perpendicular to the tube axis in $(n,0)$ tubes (see the $(n,0)$-axis direction in Figure 2(c)), and become elongated as the diameter decreases, due to the introduced curvature along their direction. The d_3 bonds have an alignment intermediate between the $\mathbf{a}_1$ and $\mathbf{a}_2$ vectors of the parent sheet, and do not suffer strong variations as we vary tube diameter. Conversely, the d_5 bonds tend to shorten in narrow tubes, as they are more closely aligned with the tube axis. These trends for d_1, d_4, and d_5 are reversed for $(0,m)$ tubes (see the $(0,m)$-axis direction in Figure 2(c)), since now d_1, d_4 are along the tube axis (and shorten for small diameters), and d_5 (as well as d_3) are elongated due to higher curvature. However, at large diameters, the bond lengths for the different chiralities tend to have a common value. In general, curvature effects on bond lengths become significant for nanotubes with diameters $D < 7$ Å. As expected, the strong curvature associated with small diameters leads to distortions in both bond angles and lengths. As we will discuss below, this imposes a higher energetic cost on maintaining structural stability. For larger diameters, the bond-length variations do not exhibit significant fluctuations, as verified for both chiralities.

Energetic Stability

We analyze the structural stability of a nanotube relative to its 2D parent allotrope considering the curvature energy (E_C), which is the variation in total energy when the sheet is rolled to form the nanotube. For this analysis, shown in Figure 3, we define the curvature energy as being

$$E_C = \frac{E_{1D}}{N_{1D}} - \frac{E_{2D}}{N_{2D}} \quad (3)$$

where E_{1D} and E_{2D} (N_{1D} and N_{2D}) are the total energies (number of atoms) in the 1D and 2D systems, respectively. Figure 3 shows E_C as a function of diameter for the two chiralities of the studied nanotubes.

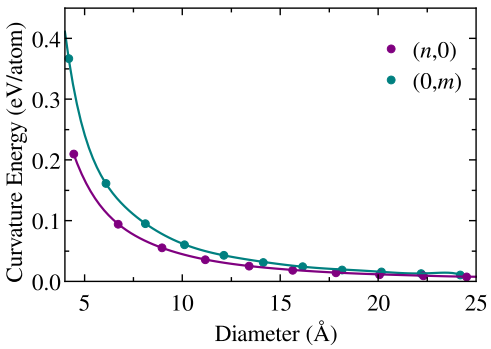

Figure 3. Curvature energy as a function of diameter for $(n, 0)$ and $(0, m)$ rγGYNTs.

https://doi.org/10.1021/acsnanoscienceau.5c00157
ACS Nanosci. Au XXXX, XXX, XXX−XXX

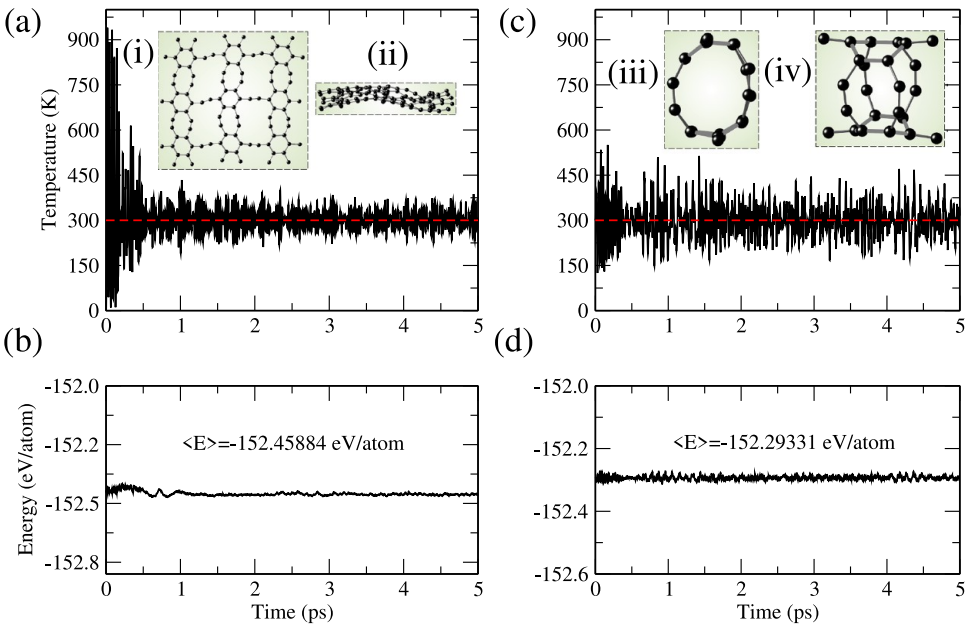

Figure 4. AIMD results for the rγGY membrane and the (0,2) nanotube at 300 K. Panels (a, c) show the temperature evolution as a function of time, while (b, d) display the corresponding total energy profiles. Insets (i−iv) illustrate representative atomic configurations during the simulations for both systems.

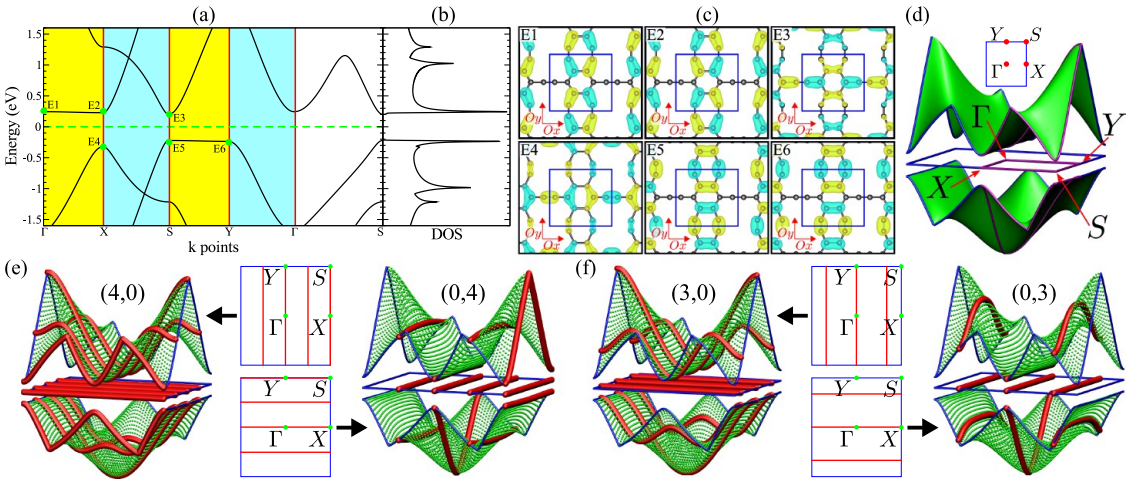

Figure 5. (a) Electronic structure of rγGY represented over high-symmetry lines of the Brillouin zone (BZ). The yellow (cyan) shaded areas represent the k-space paths parallel to the $\mathbf{b}_1$ ($\mathbf{b}_2$) vector of the reciprocal lattice. E1−E6 represent important energy levels from the frontier bands. (b) Density of states of rγGY. (c) Real part of the wave function for the E1−E6 energy levels indicated in (a), with cyan and yellow clouds representing portions of the wave function with opposite sign. (d) Valence and conduction bands of rγGY are represented by a surface plot over the entire BZ, with the Fermi energy represented by the blue rectangle. (e) Cutting lines for the (4,0) and (0,4) tubes represented over the 2D BZ and over the frontier bands of rγGY. (f) Same as (e), but for the (3,0) and (0,3) tubes.

Considering small diameters, the (n,0) family reveals a lower curvature energy compared to the (0,m) family, indicating that rolling the membrane in the x direction requires less energy than rolling the sheet in the y direction (see Figure 1(a)). This preferential energetic direction can be explained by the structural and electronic anisotropy of the 2D sheet, which affects its rigidity to curve in different directions. In other words, the energy required to roll up the material depends on the crystallographic direction chosen, and this is directly related to the way the orbitals and carbon bonds are arranged in the plane. In particular, curvature in (0,m) tubes affects mostly CABs, highlighting the locally less stable environment of these sp atoms, which deviate significantly from their ideal linear geometry. For larger diameters, E_C tends to zero, acquiring values lower than k_{BT} at room temperature already for the wider tubes considered in this work. This further indicates that the membrane is the ground state for the rγGY lattice and that the energy cost of rolling the sheet into a nanotube becomes negligible as the radius increases. This behavior arises from the fact that, for small curvatures, the energy variation approximately follows a quadratic law $E_C \propto 1/R^2$, where $R = d_t/2$ is the nanotube radius, and the energy difference between the flat and cylindrical configurations disappears when $R \rightarrow \infty$. In summary, the lower bending energy for the (n,0) family results from the mechanical anisotropy of the membrane, indicating that the x direction has a lower curvature modulus than the y direction. This indicates that the crystal lattice, its angular distribution of bonds, and

https://doi.org/10.1021/acsnanoscienceau.5c00157
ACS Nanosci. Au XXXX, XXX, XXX−XXX

electronic hybridization favor smoother deformations when the rolling occurs in this orientation.

Thermal Stability

To further assess thermal stability under the most critical conditions, we performed *ab initio* molecular dynamics (AIMD) simulations for the highest-curvature system considered in this work, namely the (0,2) nanotube, along with its 2D counterpart for comparison. The simulations were carried out within the NVT ensemble using a Nosé thermostat, with a time step of 1 fs and a total simulation time of 5 ps at 300 K. The results are presented in Figure 4. The temperature evolution for the 2D membrane and the nanotube, shown in Figure 4(a,c), reveals that after a short initial thermalization stage, both systems fluctuate around the target temperature with comparable amplitudes, indicating proper equilibration and stable sampling of the canonical ensemble. The nanotube exhibits slightly larger instantaneous fluctuations, which can be attributed to curvature-induced local strain and reduced symmetry. The total energy profiles, displayed in Figure 4(b,d), show that in both cases the energy oscillates around a well-defined average value with no observable drift, confirming the numerical stability of the integration scheme and the absence of thermal degradation. As expected, the average energy per atom of the nanotube is higher than that of the 2D membrane, reflecting the energetic cost associated with curvature, in full agreement with the curvature energy analysis discussed above. From a structural perspective, the representative snapshots in Figure 4(i−iv) show that both systems preserve their bonding topology throughout the simulation. Although small distortions in bond lengths and angles are observed, particularly in the nanotube, no bond breaking or reconstruction processes occur. Since the (0,2) nanotube corresponds to the smallest diameter and highest-curvature configuration considered here, its demonstrated thermal stability indicates that all larger-diameter nanotubes, which are energetically more favorable and less strained, are expected to be at least equally or more stable under similar thermal conditions.

Electronic Structure of Nanotubes

Before discussing the electronic structure of nanotubes, it is essential to revisit the electronic structure of the rγGY sheet. In Figure 5(a), we illustrate its electronic band structure represented along the high-symmetry lines of the rectangular Brillouin zone (BZ), followed by the corresponding density of states (DOS) in Figure 5(b). The valence band exhibits a flat sector along the $S-Y$ path, as well as a dispersive sector with a local maximum value at the X point, which has a value slightly below that of the flat sector. The flat sector results in a prominent peak in the DOS plot at the valence band maximum (VBM) position, which is followed by a shoulder-shaped peak in the energy value of the local maximum at the X point. A similar picture is observed for the conduction band, but with a flat sector along the $\Gamma-X$ path. Further, the dispersive sector of the conduction band has a minimum value at the S point of the BZ, which is the global minimum of the band, but with an energy very close to that of the flat sector. The flat sector also results in a pronounced van Hove singularity at the conduction band minimum (CBM) (as visible from the DOS plot), and the global minimum of the valence band shows up as a small shoulder close below the CBM peak. All these features are in agreement with the previous study on the rγGY sheet.[40]

There are a few energy levels of the valence and conduction bands that deserve special attention, namely those marked by the green circles labeled as E1, E2, E3, E4, E5, and E6 in Figure 5(a). Such points will be relevant to understanding the electronic properties of rγGYNTs, as discussed later. In Figure 5(c), we plot the real part of the wave functions of these levels over the rγGY sheet, where the cyan and yellow sectors of the plots represent opposite signs of the wave function. The E1 and E2 levels lie at the Γ and X points of the BZ, respectively, both on the flat sector of the conduction band. They have very similar spatial distributions over the bonds involving (1) a sp^2 atom from the hexagonal rings and (2) a sp atom from the CABs along the $\mathbf{a}_2$ direction. They basically differ by the phase difference between neighboring unit cells due to the Bloch phase $\exp(i\mathbf{k}\cdot\mathbf{R})$ (where i is the imaginary unit, $\mathbf{k}$ the vector from the BZ, and $\mathbf{R}$ a lattice vector). While the E1 wave function (at Γ) has the same phase for all unit cells, the E2 wave function (at X) inverts its sign for neighbor cells along the $\mathbf{a}_1$ direction, but not along $\mathbf{a}_2$. These wave functions are very similar to the local DOS (LDOS) plots from rγGY over the flat sector of the conduction band.[40] A similar finding is observed when we plot the real part of the wave function for the E5 (at S) and E6 (at Y) levels from the flat sector of the valence band. These levels also distribute over the 8-carbon rings from rγGY, as E1 and E2, but on complementary sets of bonds relative to E1/E2. Again, while the spatial distributions of E5 and E6 are similar to each other, they differ in their phases as we move over neighboring unit cells of the system. An explicit characteristic of the E1, E2, E5, and E6 states (from the flat sectors of the frontier bands) is their negligible contribution over the SABs aligned with the $\mathbf{a}_1$ direction of rγGY, as reported before,[40] while the other two curved acetylenic bridges in the unit cell carry a significant contribution from these states. On the other hand, the E3 and E4 states are extreme values of the dispersive sectors of the conduction and valence bands, respectively, and exhibit significantly different distributions compared to the states from the flat bands. Namely, both E3 and E4 spread over the straight acetylenic bridges along the $\mathbf{a}_1$ direction, but on complementary sets of bonds relative to each other. As a result, we can easily identify the origin of a given frontier state (either from a flat or dispersive band sector) by looking at details of its spatial distributions. Namely, states E1, E2, E5, and E6 spread mainly on the CABs from rγGY (and on the neighboring sp^2 sites from the hexagonal rings), while E3 and E4 primarily spread on the SABs from rγGY (and on the neighboring sp^2 sites from the hexagonal rings). To simplify later discussions, we will extend the reference to acetylenic bridges along the $\mathbf{a}_1$ ($\mathbf{a}_2$) direction of rγGY as SABs (CABs) and also to the nanotube counterparts.

The reason for revisiting the rγGY sheet is that many aspects of the electronic structure of nanotubes can be understood from the band structure of the parent sheet by a zone folding (ZF) description. The ZF approach basically consists of (1) defining cutting lines over the BZ of the 2D system, (2) computing the electronic bands of the sheet for the k-points along these lines, and (3) using the last result as an approximation for the tubes' electronic band structures. Curvature effects in ZF are only indirectly considered, as the length and spacing for the set of cutting lines are determined by specific boundary conditions for each (n,m) tube. At the same time, the ZF band values are still extracted from the Hamiltonian of the planar parent structure. For this reason,

https://doi.org/10.1021/acsnanoscienceau.5c00157
ACS Nanosci. Au XXXX, XXX, XXX−XXX

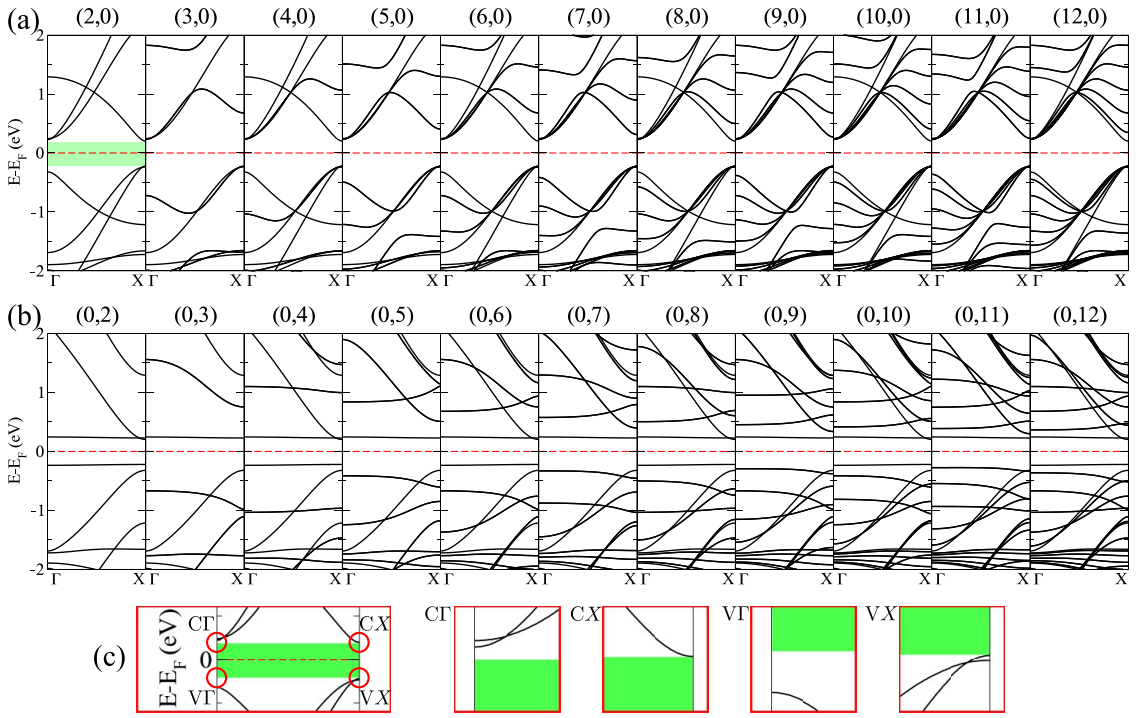

Figure 6. (a) Electronic band structures of the $(n,0)$ nanotubes, with n from 2 to 12, according to the zone-folding approach. The dashed red lines at $E = 0$ indicate the Fermi level. (b) Same as (a), but for the $(0,m)$ nanotubes, with m from 2 to 12. (c) Insets of the frontier states of the valence and conduction bands of the (2,0) tube, with the gap energy region highlighted in green.

such an approach usually fails to give reasonable results for high-curvature tubes. Even so, ZF allows us not only to rationalize the results for very wide tubes, but also to understand how the tube's properties evolve as the diameter increases from narrow tubes.

In Figure 5(d), we show the valence and conduction bands of rγGY over the entire BZ by a surface plot, where we easily identify the flat and dispersive sectors of these bands. For the (n,m) nanotube based on the rγGY sheet, the cutting lines over the reciprocal space are given by the vectors $\mathbf{k}$ of the form

$$\mathbf{k} = j\mathbf{K}_1 + \lambda\mathbf{K}_2 \tag{4}$$

where $\mathbf{K}_1$ and $\mathbf{K}_2$ are the reciprocal lattice vectors corresponding to $\mathbf{C}_h$ and $\mathbf{T}$ from direct space, respectively. The integer j index varies from 0 to $N - 1$ (N being the number of unit cells of the 2D system that fit within the unit cell of the nanotube) and $-1/2 < \lambda \leq 1/2$.[13,48]

The cutting lines for a $(n, 0)$ armchair nanotube are parallel to the $\Gamma-Y$ and $X-S$ directions of the 2D BZ. The band structure along these paths is highlighted by the cyan shaded areas in the band structure from Figure 5(a). In the upper-central part of Figure 5(e), we illustrate the cutting lines of a (4,0) nanotube over the rγGY BZ. In the left-hand side of Figure 5(e), we further show the projection of these (4,0) lines over the band structure of rγGY. From a ZF perspective, we expect a set of N ($N = n$ for the $(n,0)$ tube) conduction bands to be almost degenerated at the Γ point, as all cutting lines cross the k-space line (Γ to X) of the flat sector of the conduction band. In particular, the (4,0) tube has a feature shared with all the $(n, 0)$ nanotubes with even n: a cutting line passing along the $X-S$ path (see Figure 5(e)). This is a relevant property, since the global minimum of the conduction band lies at the S point, in the dispersive sector of the band. Conversely, odd n nanotubes lack a cutting line at the edge of the 2D BZ (see the (3,0) tube in Figure 5(f)). In the ZF picture, the set of N nearly degenerated conduction bands at the Γ point is present in all $(n,0)$ tubes, but in the odd-n case, this set usually defines the CBM. On the other hand, in $(n,0)$ armchair nanotubes with even n, the CBM lies at the BZ edge (S point in the 2D system, corresponding to the X point in the nanotube BZ) due to the $j = n/2$ cutting line. We note that for odd n, there is no cutting line passing through the $X-S$ path; however, when n is sufficiently large, the line closest to this path may intersect the dispersive part of the conduction band at a point very close to S, at an energy lower than that of the flat portion of the same band. These aspects can be further seen from the ZF-calculated band structures for $(n,0)$ rγGYNT shown in Figure 6(a) for n from 2 to 12. We note that the local minimum of the conduction band at X for odd n tubes moves toward the Fermi energy as we increase tube diameter, but even the widest odd n tube of this series still has the CBM at the Γ point. On the other hand, all even n tubes have the CBM at the edge of the BZ, coming from the $j = N/2$ cutting line.

For the valence band, we also have N almost degenerated valence bands, but now at the edge of the tube's BZ (X point of the 1D BZ). Similarly to the conduction band, this occurs because all cutting lines cross the $Y-S$ path, where the flat sector of the valence band lies. This corresponds to the system's VBM for all n values, as per ZF. Also, in the even n cases, the $(n,0)$ tubes will feature a lower valence ZF band with a maximum at Γ, differently from the odd n cases, as exemplified by the cases (4,0) and (3,0) in Figure 5(e,f), respectively. In summary, the ZF approach predicts dispersive valence and conduction bands for armchair rγGYNTs, with these bands featuring maxima (for the valence band) and minima (for the conduction band) at both the center and the edge of the 1D BZ. Physically, this dispersive character of the nanotubes bands is compatible with the delocalization of 2D

https://doi.org/10.1021/acsnanoscienceau.5c00157
ACS Nanosci. Au XXXX, XXX, XXX−XXX

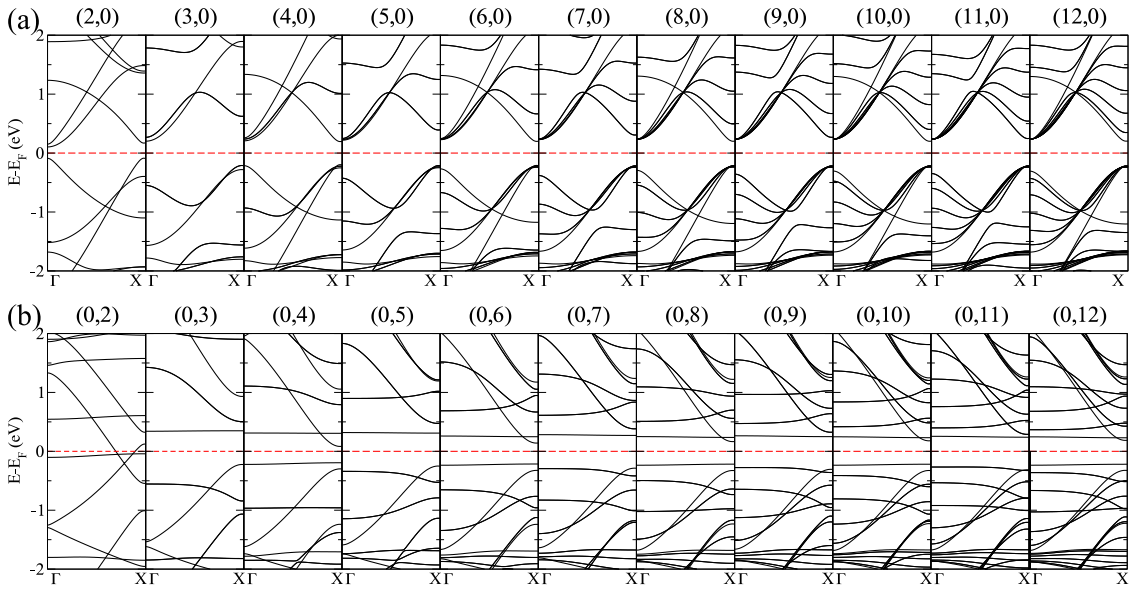

Figure 7. (a) Electronic band structures of the (n, 0) nanotubes, with n from 2 to 12, according to explicit DFT calculations (including a previous geometry optimization). The dashed red lines at E = 0 indicate the Fermi level. (b) Same as (a), but for the (0, m) nanotubes, with m from 2 to 12.

rγGY frontier states, which spread like quasi-1D states along the $\mathbf{a}_2$ direction of the sheet (the same direction of the armchair nanotubes axis). From the ZF results in Figure 6 for (n,0) tubes with n from 2 to 12, we can summarize that the CBM is always at X for even n, while the conduction band value at X is shifted up for the odd n cases, with the CBM coming from the Γ point. These aspects are further highlighted for the (2,0) case in Figure 6(c), where we amplify the conduction bands at Γ and X in the upper close vicinity of the band gap. For the VBM, it always comes from the X point, but the value of the valence band at Γ approaches (moves downward from) the VBM for even (odd) n. This is also highlighted for the (2,0) case in Figure 6(c), where we amplify the valence bands maxima at Γ and X in the lower close vicinity of the band gap. Making a further comparison with the 2D parent system, even n (n,0) nanotubes have their CBM originating from the E3 level of the sheet (S point of the 2D BZ, X point of the 1D BZ), while the CBM from odd n cases arises from E1/E2-like states (Γ−X line of the 2D BZ, Γ point of the 1D BZ). For the VBM, it always originates from the E5/E6-like 2D levels (Y−S line of the 2D BZ, X point of the 1D BZ), while a lower local valence band maximum originates from E4 (X point of the 2D BZ, Γ point of the 1D BZ). In this way, the ZF calculated band gap for even n (n,0) tubes is always the same as that of the 2D counterpart (∼ 0.42 eV), while it is a little wider for odd n cases (∼0.45 eV at least up to the n = 11 case).

In the (0, m) cases, the cutting lines are now parallel to the Γ−X and Y−S paths. These are the paths along which we observe the flat sectors of the rγGY's frontier bands, as highlighted by the yellow shaded areas in the band structure of rγGY in Figure 5(a). We always expect a flat conduction band for (0,m) tubes according to ZF, since we always have a cutting line along Γ−X (j = 0). However, for even m cases, we also have a cutting line along Y−S, and a high-dispersive conduction band crosses the flat band, resulting in the system's CBM close to the nanotube's X point. In the odd m cases, such a crossing line is absent, and the system's CBM typically originates from the flat band (except for huge tubes, which have a high density of cutting lines). Even for the widest odd m system we investigated, the CBM still comes from the flat band. These features can be observed in Figure 5(e,f), where we show the cutting lines and the corresponding projection of the 2D bands for the (0,4) and (0,3) nanotubes, respectively. For the valence band, ZF always predicts a dispersive band with its maximum at the BZ's edge, originating from the zeroth cutting line. This band typically contains the VBM in the odd m cases, whereas the VBM originates from another flat band that appears in the even m cases, due to the cutting line passing by Y−S. In Figure 6(b), we show the band structures obtained by ZF for the (0,m) tubes with m from 2 to 12. We observe that there is always a conduction flat band. But the CBM lies at such a nondispersive band only in the odd m cases, while the minimum of the high-dispersive conduction band at X is the CBM for even m, as it crosses the flat branch. For the occupied states, we have a flat valence band (containing the system's VBM) for the even m cases. Such a band is absent for odd m and the maximum value of a dispersive valence band at X is the VBM. Even though the flat band of the cutting line along Y−S is absent in odd m, another band, which is flat over most of the 1D BZ, starts to develop for large m, as the density of cutting lines increases and we have a line close to (but not at) the Y−S path. Such a partially flat band in odd m cases gradually approaches the dispersive VBM, while they eventually cross each other at (0,9), where the CBM now comes at Γ from the low-dispersive band. In summary, the CBM in odd m cases usually comes from E2 states from rγGY (which are slightly below E1 levels), while it comes from the E3 state for even m. Conversely, the VBM comes from the E5 states (a little higher in energy compared to E6) for even m, while it comes from the E4 state for odd m (or from a state close to E5 for large m values). In this way, ZF predicts that (0,m) tubes with even m to have the same gap as the 2D counterpart, while it is a little wider (at most ∼0.55 eV) for odd m cases.

We note that ZF yields more accurate results for very large tubes. Although qualitative considerations can be made for narrow tubes based on ZF, it fails to provide precise bands

https://doi.org/10.1021/acsnanoscienceau.5c00157
ACS Nanosci. Au XXXX, XXX, XXX−XXX

when a high curvature occurs. In this way, especially for small-diameter tubes, it is crucial to proceed with explicit simulations that involve geometry optimization and further computation of the bands for these cylindrical materials.

In Figure 7(a), we show the electronic band structure for the $(n,0)$ nanotubes calculated from an explicit DFT calculation. We note that the DFT results agree with the ZF data in qualitative terms, even for narrow tubes. We also observe a reasonable quantitative agreement for wider tubes. In general, the explicit effect of curvature is to move the DFT frontier bands closer to the E_F compared to the ZF picture, resulting in overall smaller gaps. The (2,0) tube is the one featuring the major DFT-ZF differences, even though ZF is still able to predict the semiconducting character of the tube, with (2,0) DFT (ZF) gap being 0.19 eV (0.42 eV). Another DFT-ZF difference in the (2,0) case is that the CBM arrives at the Γ point in DFT, instead of at X as expected from ZF. Furthermore, the set of almost degenerate conduction (valence) bands at Γ (X) is also lifted in the (2,0) tube, a feature also easily noticeable in the (3,0) case, while this effect fades away as the tube diameter increases. In Figure 8 we plot

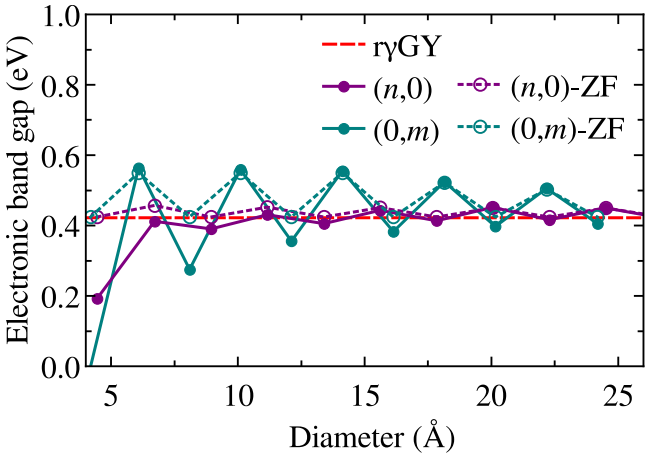

Figure 8. Electronic band gap of $(n,0)$ (purple lines) and $(0,m)$ (green lines) rγGY nanotubes as a function of tube diameter according to the ZF (empty circles with dashed lines) and DFT (filled circles with full lines) approaches. The horizontal red dashed line indicates the 2D rγGY reference value.

the band gap of the $(n,0)$ tubes as a function of tube diameter according to the DFT and ZF approaches. The DFT results maintain the even−odd oscillations predicted by ZF. We gradually observe a better performance of ZF predicting the band gap, as the even n DFT series shows a gap within an 11 meV difference to that of the 2D counterpart value for $n \geq 8$. On the other hand, except for the $n = 3$ case, all tubes from the odd series feature a gap larger than the 2D case (a ZF prediction), while the DFT-ZF difference in the band gap value lies below 0.1 eV for $n \geq 7$.

In Figure 9, we illustrate particular levels from the (2,0) by plotting two side views of the real part of their wave functions. Here, we consider a phase choice in which the imaginary part vanishes. We plot the wave functions for the highest valence (−1) and for the first two conduction bands (+1 and +2) at the Γ point, as well as for the highest two valence (−2 and −1) and for the conduction (+1) band at the X point of the 1D BZ. We note that the valence band wave function at Γ and the conduction band wave function at X (both in the 1D BZ) hold

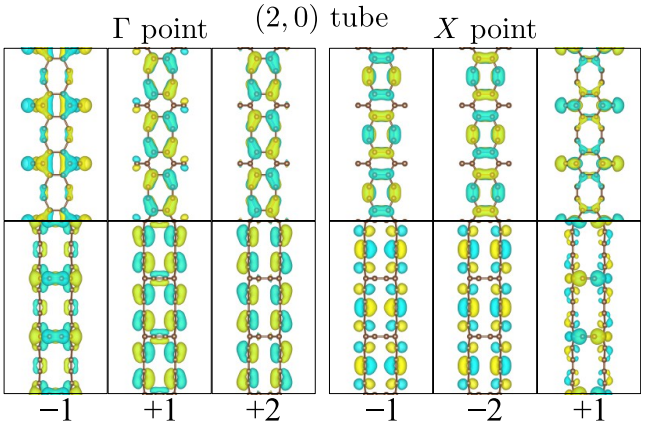

Figure 9. Real part of the wave functions of the (2,0) tube for the highest valence band (−1) and for the two lowest conduction bands (+1 and +2) at the Γ point, as well as for the highest two valence bands (−2 and −1) and for the lowest conduction band (+1) at the X point of the 1D BZ.

similarities with the E4 and E3 states in the 2D counterpart, which is consistent with the ZF association between tube and 2D levels. Furthermore, E4/E3 in rγGY lies at the X/S point of the 2D BZ, while we note that the $\mathbf{b}_1$ component of these wavevectors is 1/2 ($\mathbf{b}_1$ being the rγGY reciprocal lattice vector along the $\mathbf{a}_1$ direction of the sheet). In the 2D system, the E4/E3 wave functions change sign as we move to neighboring cells along $\mathbf{a}_1$, recovering the original phase for even multiples of such a displacement. This is compatible with the geometry of the (2,0) tube, as it has two rγGY unit cells around its circumference. On the other hand, the wave functions for the first two conduction bands at Γ have very similar features compared to the E1/E2 states from the sheet. While these tube states do not change sign when moving between neighboring cells along the axis (a Γ point feature), the +1 (+2) wave function does not change (change) sign for successive rγGY cells along the circumference, consistent with the symmetry of their originating k-vectors in the 2D system. In the +1 case, we note that the atoms from the SABs have a significant contribution resulting from curvature. Such an amplitude on the SABs resembles p orbital lobes orthogonal to the plane containing the C−C bonds, different from the rest of the structure, where the π-like clouds are somehow orthogonal to the tube surface. Similarly, the spatial distribution of the valence −1 and −2 states at the tube X point confirms their origin from the E6/E5 of the parent sheet, as well as the +1 state compared to E3.

In Figure 7(b), we show the electronic band structure for the $(0,m)$ nanotubes calculated from an explicit DFT calculation. These results agree well with the ZF data in qualitative terms for most cases. The only exception is the (0, 2) tube, which is predicted as being metallic within DFT. This is the only system among the studied rγGY nanotubes that exhibits metallic behavior. We point out that this arises from strong curvature effects. Notably, this system shows the largest discrepancy between the DFT-calculated band structure and the ZF result, indicating that curvature plays a dominant role in determining its electronic signature. Such a breakdown of the ZF description (which indicates the onset of strong curvature effects) has also been reported for graphene-based nanotubes.[49] It originates from significant mixing between σ and π carbon orbitals, which ultimately leads to the metallic behavior

https://doi.org/10.1021/acsnanoscienceau.5c00157
ACS Nanosci. Au XXXX, XXX, XXX−XXX

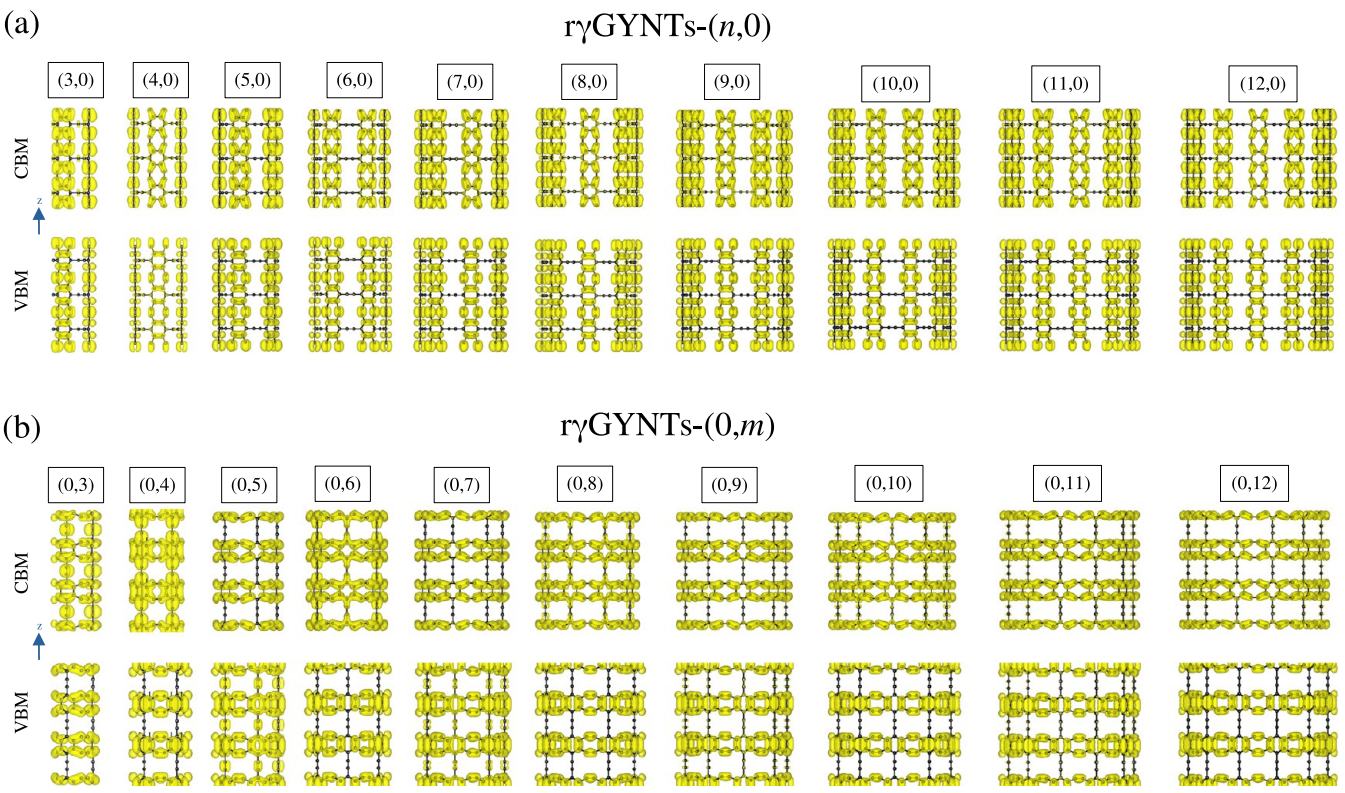

Figure 10. (a) LDOS plots for the VBM and CBM levels of the (*n*,0) rγGYNTs with *n* from 3 to 12. (b) Same as (a), but for (0,*m*) rγGYNTs with *m* from 3 to 12.

observed in very small graphene nanotubes, as in the (0,2) rγGY nanotube. Overall, for the (0,*m*) tubes with $m > 2$, the flat (dispersive) conduction band is shifted away (toward) the Fermi energy, while both flat and dispersive valence levels shift closer to the E_F. This results in DFT gaps generally narrower than the corresponding ZF values. Such an effect reaches its maximum strength in the $m = 2$ case, resulting in bands that cross the Fermi level. Even in this case, the DFT results still capture the pair of flat bands predicted from ZF. For the even *m* series, all tubes are predicted to have the same gap as the 2D systems according to ZF, whereas we observe that the DFT-predicted gap approaches that of the 2D rγGY at a slower rate compared to the (*n*,0) nanotubes. We can rationalize this in terms of the positions of the acetylenic chains relative to the axis of the tube. We note that the CABs lie around the tube circumference in (0,*m*) tubes and are more affected by curvature than the SABs (which lie along the axis). This is the other way around for the (*n*,0) cases. Since (0,*m*) tubes have two CABs for each SAB, they are expected to be more affected by curvature than (*n*,0) systems, which is consistent with the even *n* cases approaching the gap of the 2D systems at a faster pace than the even *m* tubes.

To further illustrate the similarity between the ZF and DFT results, in Figure 10 we present the local density of states (LDOS) plots for the VBM and CBM states of the (*n*,0) and (0,*m*) rγGYNTs, with *n* and *m* ranging from 3 to 12. To integrate the LDOS along the energy axis, we considered an interval of 0.01 eV around the VBM/CBM energy value. The results allow us to analyze the electronic distribution of their frontier states along the different structural arrangements. As discussed for the (*n*,0) tubes, their CBM originates from dispersive (flat) bands of the 2D counterpart for even (odd) *n*. In this sense, we would expect that the CBM of (*n*,0) tubes would resemble the E3 (E1/E2) states in even (odd) *n* systems. However, these levels are very close in energy on the 2D parent system and in their 1D counterparts with an even *n* index, so that both tube levels are summed up once we integrate the LDOS over the 0.01 eV interval. And since conduction (E1/E2-like) states feature a much higher DOS contribution, they dominate the CBM LDOS profile for all (*n*,0) tubes, as observed in Figure 10(a). On the other hand, the VBM in the (*n*,0) tubes always comes from the flat branch of the originating 2D layer, so the VBM for all these tubes looks like the E5/E6 2D states.

For the (0,*m*) tubes, the even−odd alternation clearly shows up in the LDOS profiles. For even *m* tubes, their VBM originates from the 2D dispersive valence band, so that the tubes' LDOS has a strong participation of the SABs (see Figure 10(b)), a feature from the 2D E3 level. For odd cases, the CBM originates from the flat bands, and their LDOS clearly resembles the spatial distribution of the E1/E2 2D states. Regarding the VBM, it always comes from the flat band in even *m* tubes, and their LDOS plots have a similar profile when compared to the 2D E5/E6 states. This is different for the odd *m* tubes, as the VBM originates from the dispersive 2D valence band (E4) states. As we look at the (0,3) and (0,5) tubes, there is a strong participation of the SAB atoms (a feature of the 2D E4 states). However, as we increase the tube diameter, the flat sector of the valence band approaches the VBM and gradually becomes closer to the VBM in odd *m* systems (see Figure 7(b)), entering the energy range used for LDOS integration. So, starting from the (0,7) system to wider tubes, the relative LDOS contribution from the SAB atoms becomes less noticeable, and we observe a charge profile closer to that of

https://doi.org/10.1021/acsnanoscienceau.5c00157
ACS Nanosci. Au XXXX, XXX, XXX−XXX

the 2D E5/E6 states, as the flat portion of the tubes' valence bands provides a much larger contribution to the total DOS.

We point out that the PBE results here reported for band gaps have to be considered as lower threshold reference values. This is because the PBE functional is well-known to underestimate band gaps, whereas hybrid functions are expected to give more accurate gap values, as verified, for instance, for 2D rγGY.[40] We remark, however, that the PBE functional can capture the essence of the physical mechanisms in these materials. In the particular case of the (0,2) nanotube, its NP configuration is the only metallic system found in this study. To make sure this is not an artifact of the method, we also simulated this system using the Heyd-Scuseria-Ernzerhof (HSE06) exchange-correlation functional,[50,51] as implemented in the HONPAS (Hefei Order-N Packages for Ab Initio Simulations) package.[52,53] In Figure 12, we show the electronic band structure of the (0,2) tube in its NP configuration as predicted by this hybrid functional. While we note that the flat levels observed in the PBE result are slightly shifted away from the Fermi level with the hybrid functional, the other two dispersive bands continue to cross E_F, confirming the metallic behavior found in the PBE calculation. To assess the band gap underestimation, we simulated the (0,3) and (3,0) tubes as representative examples. The results are also shown in Figure 12. These systems are found to be semiconductors, with the computed band gaps being 1.16 eV, and 0.99 eV, with values larger than the corresponding PBE results. However, the bands are qualitatively similar to those obtained with the PBE functional.

We finish discussing another feature of the (0,2) tube: a flat band very close to the Fermi level. In other systems that share this characteristic, it is very common to observe the occurrence of spin-polarized (SP) states.[21] In addition, a SP configuration emerges in systems with structural similarity to rγGY, such as 2D biphenylene[54] and a rectangular α-GY-like version of biphenylene.[39] In the last case, the 2D system has flat levels like the ones shown by rγGY, but such levels in the rectangular α-GY system lie much closer to E_F than in rγGY (which does not feature such a SP configuration). For this reason, we further performed spin-polarized calculations for the (0,2) tube, which revealed that it hosts a nontrivial spin electronic distribution. In Figure 11 we show the electronic band structure of the SP state of the (0, 2), where blue full (red dashed) lines represent spin-up (spin-down) bands. We also reproduce the band structure of the corresponding non-polarized (NP) state (black full lines, also previously shown in Figure 7). The SP state is a semiconducting configuration, as it shifts the valence flat band outward of the Fermi level, and lifts (by 0.54 eV) the crossing degeneracy of the two dispersive bands from the NP case. However, the band gap of the system is between the flat valence band and the upper dispersive branch (0.25 eV). The difference between the spin-up and spin-down components of the electronic charge is further illustrated by the plot in Figure 11, where regions with an excess of spin-up (spin-down) are illustrated by blue (red) color clouds. We note that each atom with a majority spin-up is neighboring to atoms with a majority spin-down, resulting in a configuration with a zero total magnetic moment. The onsite spin orientations are compatible with the bipartition of the atomic structure, similar to what happens with 2D biphenylene and the rectangular α-GY based on biphenylene. The SP configuration shown in Figure 12 is also the system's ground state by an 88 meV difference.

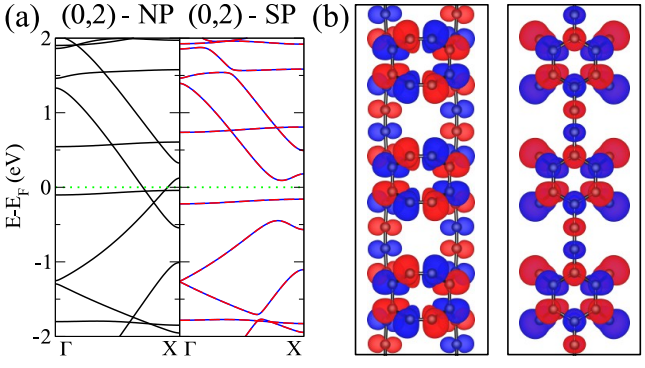

Figure 11. (a) Electronic band structure of the (0,2) tube in its NP (black full lines) and SP (blue full/red dashed lines for spin-up/spin-down) configurations. Dotted green lines represent the Fermi energy. (b) Spin-polarization plot for the SP state of the (0,2) tube, with blue/red clouds representing regions with an excess of spin-up/spin-down electrons.

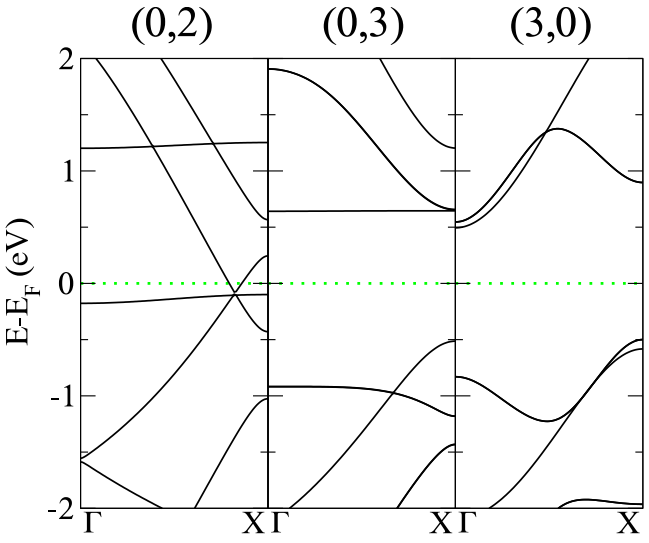

Figure 12. Electronic band structure of the (0,2), (0,3), and (3,0) systems in their NP configuration according to simulations based on the HSE06 exchange-correlation functional. In all cases, the dotted green line at $E = 0$ represents the Fermi energy.

CONCLUDING REMARKS

In summary, we investigated the electronic properties of carbon nanotubes based on a rectangular graphyne sheet. In general, large-diameter tubes closely follow the properties of their parent sheet, as these tubes are also semiconducting. The overall profiles of the band structures of low-curvature tubes are well described in terms of a zone-folding approach, which rationalizes the resemblance between the electronic signatures of tubes and their originating sheets. However, curvature acts as a way to modulate the tubes' band gap, especially for tubes with the (0,m) chirality, as the folding direction structurally affects mainly acetylenic bridges strongly associated with the frontier states of the original 2D system. Strong gap modulation also occurs for narrow nanotubes, including a case where a nanotube becomes metallic. This last structure undergoes a further transition to a semiconducting state due to its spin-polarized configuration. A special advantage of

https://doi.org/10.1021/acsnanoscienceau.5c00157
ACS Nanosci. Au XXXX, XXX, XXX−XXX

rγGYNTs is that they are systematically semiconductors, regardless of their chirality, a distinct feature compared to graphene-based nanotubes, which are semiconducting only under specific structural conditions.

AUTHOR INFORMATION

Corresponding Author

Eduardo Costa Girão − *Departamento de Física, Universidade Federal do Piauí, Teresina 64049-550 Piauí, Brazil;* orcid.org/0000-0001-9005-9484; Email: edu@ufpi.edu.br

Authors

Wjefferson Henrique da Silva Brandão − *Institute of Physics, Fluminense Federal University, Niterói 24210-340 Rio de Janeiro, Brazil;* orcid.org/0000-0003-2832-9687

Anderson Gomes Vieira − *Departamento de Física, Universidade Federal do Piauí, Teresina 64049-550 Piauí, Brazil*

Jonathan da Rocha Martins − *Departamento de Física, Universidade Federal do Piauí, Teresina 64049-550 Piauí, Brazil*

Andrea Latgé − *Institute of Physics, Fluminense Federal University, Niterói 24210-340 Rio de Janeiro, Brazil;* orcid.org/0000-0002-8152-6455

Marcelo Lopes Pereira, Junior − *University of Brasília, College of Technology, Department of Electrical Engineering, Brasília 70910-900, Brazil;* orcid.org/0000-0001-9058-510X

Complete contact information is available at: https://pubs.acs.org/10.1021/acsnanoscienceau.5c00157

Funding

The Article Processing Charge for the publication of this research was funded by the Coordenacao de Aperfeicoamento de Pessoal de Nivel Superior (CAPES), Brazil (ROR identifier: 00x0ma614).

Notes

The authors declare no competing financial interest.

ACKNOWLEDGMENTS

W.H.S.B. acknowledges the Carlos Chagas Filho Research Support Foundation of the State of Rio de Janeiro (FAPERJ) for financial support under grants E-26/200.146/2024 and E-26/200.147/2024. M.L.P.J. acknowledges financial support from FAPDF (grant 00193-00001807/2023-16), CNPq (grants 444921/2024-9 and 308222/2025-3), and CAPES (grant 88887.005164/2024-00). E.C.G. acknowledges support from CNPq (Process No. 309832/2023-3) and from the Laboratório de Simulação Computacional Cajuína (LSCC) at Universidade Federal do Piauí. The authors acknowledge support from the Centro Nacional de Processamento de Alto Desempenho at Ceará (CENAPAD-UFC) and São Paulo (CENAPAD-SP) in Brazil. Authors also acknowledge the NANOHEXA-UFF and NanoEng-Unb clusters for providing computational infrastructure.

REFERENCES

(1) Kroto, H. W.; Heath, J. R.; Obrien, S. C.; Curl, R. F.; Smalley, R. E. C-60 - Buckminsterfullerene. *Nature* **1985**, *318* (6042), 162−163.

(2) Iijima, S. Helical microtubules of graphitic carbon. *Nature* **1991**, *354* (6348), 56−58.

(3) Iijima, S.; Ichihashi, T. Single-shell carbon nanotubes of 1 nm diameter. *Nature* **1993**, *363* (6430), 603−605.

(4) Bethune, D. S.; Kiang, C. H.; Devries, M. S.; Gorman, G.; Savoy, R.; Vazquez, J.; Beyers, R. Cobalt-catalyzed growth of carbon nanotubes with single-atomic layerwalls. *Nature* **1993**, *363* (6430), 605−607.

(5) Hughes, K. J.; Iyer, K. A.; Bird, R. E.; Ivanov, J.; Banerjee, S.; Georges, G.; Zhou, Q. A. Review of carbon nanotube research and development: Materials and emerging applications. *ACS Appl. Nano Mater.* **2024**, *7* (16), 18695−18713.

(6) Novoselov, K. S.; Geim, A.; Morozov, S.; Jiang, D.; Zhang, Y.; Dubonos, S.; Grigorieva, I.; Firsov, A. Electric field effect in atomically thin carbon films. *Science* **2004**, *306* (5696), 666−669.

(7) Zhao, Y.; Lin, L. Graphene, beyond lab benches. *Science* **2024**, *386* (6718), 144−146.

(8) Manzeli, S.; Ovchinnikov, D.; Pasquier, D.; Yazyev, O. V.; Kis, A. 2d transition metal dichalcogenides. *Nat. Rev. Mater.* **2017**, *2*, No. 17033.

(9) Muzaffar, M. U.; Wang, X.-S.; Zhang, S.; Cui, P.; Zhang, Z. Epitaxial growth of black phosphorene enabled on black-phosphorene-like group iv-vi substrates. *Phys. Rev. B* **2021**, *104*, No. 235415.

(10) Onyancha, R. B.; Ukhurebor, K. E.; Aigbe, U. O.; Osibote, O. A.; Kusuma, H. S.; Darmokoesoemo, H.; Balogun, V. A. A systematic review on the detection and monitoring of toxic gases using carbon nanotube-based biosensors. *Sens. Bio-Sen. Res.* **2021**, *34*, No. 100463.

(11) Ferreira, M. S.; Dargam, T. G.; Muniz, R. B.; Latgé, A. Local electronic properties of carbon nanotube heterojunctions. *Phys. Rev. B* **2000**, *62*, No. 16040.

(12) Dai, H. Carbon nanotubes: opportunities and challenges. *Surf. Sci.* **2002**, *500* (1−3), 218−241.

(13) Samsonidze, G. G.; Saito, A. R.; Jorio, D. A.; Pimenta, E. M. A.; Souza Filho, E. A. G.; Grüneis, F. A.; Dresselhaus, D. G.; Dresselhaus, M. S. The concept of cutting lines in carbon nanotube science. *J. Nanosci. Nanotechnol.* **2003**, *3* (6), 431−458.

(14) Qi, P.; Javey, A.; Rolandi, M.; Wang, Q.; Yenilmez, E.; Dai, H. Miniature organic transistors with carbon nanotubes as quasi-one-dimensional electrodes. *J. Am. Chem. Soc.* **2004**, *126* (38), 11774−11775.

(15) Kleinherbers, E.; Stegmann, T.; Szpak, N. Electronic transport in bent carbon nanotubes. *Phys. Rev. B* **2023**, *107*, No. 195424.

(16) Saito, R.; Dresselhaus, G.; Dresselhaus, M. S. *Physical Properties of Carbon Nanotubes*; Imperial College Press: London, 1998.

(17) Terrones, H.; Lv, R.; Terrones, M.; Dresselhaus, M. S. "The role of defects and doping in 2d graphene sheets and 1d nanoribbons". *Rep. Prog. Phys.* **2012**, *75*, No. 062501.

(18) Lee, H.; Paeng, K.; Kim, I. S. A review of doping modulation in graphene. *Synth. Met.* **2018**, *244*, 36−47.

(19) Son, Y.-W.; Cohen, M. L.; Louie, S. G. Energy gaps in graphene nanoribbons. *Phys. Rev. Lett.* **2006**, *97* (21), No. 216803.

(20) Son, Y.-W.; Cohen, M. L.; Louie, S. G. Half-metallic graphene nanoribbons. *Nature* **2006**, *444* (7117), 347−349.

(21) Pisani, L.; Chan, J. A.; Montanari, B.; Harrison, N. M. Electronic structure and magnetic properties of graphitic ribbons. *Phys. Rev. B* **2007**, *75* (6), No. 064418.

(22) Crespi, V. H.; Benedict, L. X.; Cohen, M. L.; Louie, S. G. Prediction of a pure-carbon planar covalent metal. *Phys. Rev. B* **1996**, *53*, No. R13303.

(23) Terrones, H.; Terrones, M.; Hernandez, E.; Grobert, N.; Charlier, J.; Ajayan, P. New metallic allotropes of planar and tubular carbon. *Phys. Rev. Lett.* **2000**, *84* (8), No. 1716.

(24) Liu, Z.; Hussain, T.; Karton, A.; Er, S. Empowering hydrogen storage properties of haeckelite monolayers via metal atom functionalization. *Appl. Surf. Sci.* **2021**, *556*, No. 149709.

(25) Chen, M.; Han, X.; Tang, K. Topological regulations of stone-wales graphene. *Carbon* **2024**, *226*, No. 119163.

(26) Girão, E. C.; Macmillan, A.; Meunier, V. Classification of sp2-bonded carbon allotropes in two dimensions. *Carbon* **2023**, *203*, 611−619.

(27) Fan, Q.; Yan, L.; Tripp, M. W.; Krejčí, O.; Dimosthenous, S.; Kachel, S. R.; Chen, M.; Foster, A. S.; Koert, U.; Liljeroth, P.; Gottfried, J. M. Biphenylene network: A nonbenzenoid carbon allotrope. *Science* **2021**, *372* (6544), 852−856.
(28) Zhang, S.; Zhou, J.; Wang, Q.; Chen, X.; Kawazoe, Y.; Jena, P. Penta-graphene: A new carbon allotrope. *Proc. Natl. Acad. Sci. U.S.A.* **2015**, *112* (8), 2372−2377.
(29) Ram, B.; Mizuseki, H. Tetrahexcarbon: A two-dimensional allotrope of carbon. *Carbon* **2018**, *137*, 266−273.
(30) Malko, D.; Neiss, C.; Vines, F.; Görling, A. Competition for graphene: graphynes with direction-dependent dirac cones. *Phys. Rev. Lett.* **2012**, *108* (8), No. 086804.
(31) Ivanovskii, A. Graphynes and graphdyines. *Prog. Solid State Chem.* **2013**, *41* (1), 1−19.
(32) Wu, W.; Guo, W.; Zeng, X. C. Intrinsic electronic and transport properties of graphyne sheets and nanoribbons. *Nanoscale* **2013**, *5* (19), 9264−9276.
(33) Yue, Q.; Chang, S.; Kang, J.; Tan, J.; Qin, S.; Li, J. "Magnetic and electronic properties of α-graphyne nanoribbons". *J. Chem. Phys.* **2012**, *136*, No. 244702.
(34) Kang, B.; Lee, J. Y. Electronic properties of α-graphyne nanotubes. *Carbon* **2015**, *84*, 246−253.
(35) Mohammadi, A.; Zaminpayma, E. Armchair α-graphyne nanoribbons as negative differential resistance devices: Induced by nitrogen doping. *Org. Electron.* **2018**, *61*, 334−342.
(36) Rodrigues, D. C. M.; Lage, L. L.; Venezuela, P.; Latgé, A. Exploring the enhancement of the thermoelectric properties of bilayer graphyne nanoribbons. *Phys. Chem. Chem. Phys.* **2022**, *24*, 9324−9332.
(37) Oliveira, T. A.; Silva, P. V.; Girão, E. C. The electronic properties of non-conventional α-graphyne nanoribbons. *Phys. Chem. Chem. Phys.* **2022**, *24*, 26813−26827.
(38) Ullah, S.; Menezes, M. G.; Silva, A. M. Theoretical characterization of tolanene: A new 2d sp-sp2 hybridized carbon allotrope. *Carbon* **2024**, *217*, No. 118618.
(39) Rêgo, M. S.; dos Santos, M. R.; Junior, M. L. P.; Girão, E. C.; Meunier, V.; Silva, P. V. Structural, mechanical, and electronic properties of single graphyne layers based on a 2d biphenylene network. *Carbon Trends* **2025**, *20*, No. 100506.
(40) Vieira, A. G.; Pereira, M. L.; Meunier, V.; Girão, E. C. Electronic properties of two-dimensional rectangular graphyne based on phenyl-like building blocks. *Carbon Trends* **2024**, *16*, No. 100395.
(41) Hong, I.; Bae, H.; Ahn, J.; Shin, H.; Lee, H.; Kwon, Y. Design of biphenylene-derived tunable dirac materials. *FlatChem* **2024**, *48*, No. 100760.
(42) Hohenberg, P.; Kohn, W. Inhomogeneous Electron Gas. *Phys. Rev. B* **1964**, *136* (3B), No. B864.
(43) Kohn, W.; Sham, L. J. Self-Consistent Equations Including Exchange and Correlation Effects. *Phys. Rev.* **1965**, *140* (4A), No. A1133.
(44) Soler, J.; Artacho, E.; Gale, J.; Garcia, A.; Junquera, J.; Ordejon, P.; Sanchez-Portal, D. The siesta method for ab initio order-n materials simulation. *J. Phys.: Condens. Matter* **2002**, *14* (11), 2745−2779.
(45) Troullier, N.; Martins, J. L. Efficient pseudopotentials for plane-wave calculations. *Phys. Rev. B* **1991**, *43*, No. 1993.
(46) Anglada, E.; Soler, J. M.; Junquera, J.; Artacho, E. Systematic generation of finite-range atomic basis sets for linear-scaling calculations. *Phys. Rev. B* **2002**, *66*, No. 205101.
(47) Perdew, J. P.; Burke, K.; Ernzerhof, M. Generalized gradient approximation made simple. *Phys. Rev. Lett.* **1996**, *77*, No. 3865.
(48) Silva, P. V.; Souza Filho, A. G.; Meunier, V.; Girão, E. C. Structural and electronic properties of nanotubes constructed from fragmented fullerenes. *Carbon* **2019**, *147*, 616−627.
(49) Zólyomi, V.; Kürti, J. First-principles calculations for the electronic band structures of small diameter single-wall carbon nanotubes. *Phys. Rev. B* **2004**, *70*, No. 085403.
(50) Heyd, J.; Scuseria, G. E. Efficient hybrid density functional calculations in solids: Assessment of the heyd−scuseria−ernzerhof screened coulomb hybrid functional. *J. Chem. Phys.* **2004**, *121* (3), 1187−1192.
(51) Hummer, K.; Harl, J.; Kresse, G. Heyd-scuseria-ernzerhof hybrid functional for calculating the lattice dynamics of semiconductors. *Phys. Rev. B* **2009**, *80*, No. 115205.
(52) Qin, X.; Shang, H.; Xiang, H.; Li, Z.; Yang, J. Honpas: A linear scaling open-source solution for large system simulations. *Int. J. Quantum Chem.* **2015**, *115* (10), 647−655.
(53) Shang, H.; Li, Z.; Yang, J. Implementation of screened hybrid density functional for periodic systems with numerical atomic orbitals: Basis function fitting and integral screening. *J. Chem. Phys.* **2011**, *135* (3), No. 034110.
(54) Alcón, I.; Calogero, G.; Papior, N.; Antidormi, A.; Song, K.; Cummings, A. W.; Brandbyge, M.; Roche, S. Unveiling the multiradical character of the biphenylene network and its anisotropic charge transport. *J. Am. Chem. Soc.* **2022**, *144* (18), 8278−8285.

https://doi.org/10.1021/acsnanoscienceau.5c00157
ACS Nanosci. Au XXXX, XXX, XXX−XXX